

Multi-wavelength study of coronal waves associated with the CME-flare event of 3 November 2003

B. Vršnak¹, A. Warmuth², M. Temmer^{1,3}, A. Veronig³, J. Magdalenic¹, A. Hillaris⁴, and M. Karlický⁵

¹ Hvar Observatory, Faculty of Geodesy, Kačićeva 26, 10000 Zagreb, Croatia
e-mail: bvrsnak@geodet.geof.hr

² Astrophysikalisches Institut Potsdam, An der Sternwarte 16, 14482 Potsdam, Germany

³ Institute of Physics, University of Graz, Universitätsplatz 5, 8010 Graz, Austria

⁴ Department of Physics, University of Athens, 15784 Panepistimiopolis Zografos, Athens, Greece

⁵ Astronomical Institute of the Academy of Sciences of the Czech Republic, 25165 Ondřejov, Czech Republic

Received 1 July 2005 / Accepted 30 September 2005

ABSTRACT

The large flare/CME event that occurred close to the west solar limb on 3 November 2003 launched a large-amplitude large-scale coronal wave that was observed in $H\alpha$ and Fe XII 195 Å spectral lines, as well as in the soft X-ray and radio wavelength ranges. The wave also excited a complex decimeter-to-hectometer type II radio burst, revealing the formation of coronal shock(s). The back-extrapolation of the motion of coronal wave signatures and the type II burst sources distinctly marks the impulsive phase of the flare (the hard X-ray peak, drifting microwave burst, and the highest type III burst activity), favoring a flare-ignited wave scenario. On the other hand, comparison of the kinematics of the CME expansion with the propagation of the optical wave signatures and type II burst sources shows a severe discrepancy in the CME-driven scenario. However, the CME is quite likely associated with the formation of an upper-coronal shock revealed by the decameter-hectometer type II burst. Finally, some six minutes after the launch of the first coronal wave, another coronal disturbance was launched, exciting an independent (weak) decimeter-meter range type II burst. The back-extrapolation of this radio emission marks the revival of the hard X-ray burst, and since there was no CME counterpart, it was clearly ignited by the new energy release in the flare.

Key words. Sun: flares – Sun: coronal mass ejections (CMEs) – Sun: corona – shock waves – magnetohydrodynamics (MHD)

1. Introduction

Large flares and fast coronal mass ejections (CMEs) are frequently accompanied by large-scale large-amplitude magnetohydrodynamic (MHD) waves that propagate through the solar corona. The longest known observational signatures of such waves are type II radio bursts (Wild & McCready 1950) and $H\alpha$ Moreton waves (Moreton & Ramsey 1960).

More recently, an EUV counterpart of the Moreton wave was reported by Neupert (1989), in a way foreshadowing a revival of interest in coronal waves that began after direct imaging of the disturbances by the Extreme-ultraviolet Imaging Telescope (EIT) on the Solar and Heliospheric Observatory (SoHO). The discovery of “EIT-waves” (Thompson et al. 1998) prompted a search for wave signatures in other spectral domains. Soon, Moreton-like disturbances were revealed in soft X-rays (Narukage et al. 2002; Khan & Aurass 2002; Hudson et al. 2003; Warmuth et al. 2005), He I 10 830 Å (Gilbert et al. 2001; Vršnak et al. 2002; Gilbert & Holzer 2004), microwaves (Warmuth et al. 2004a; White & Thompson 2005), metric-range heliograms (Vršnak et al. 2005), etc. For an overview

and historical background see, e.g., Zhukov & Auchère (2004), Cliver et al. (2005), Vršnak (2005), Warmuth (2005).

Moreton waves and type II bursts are very closely related phenomena (e.g., Harvey et al. 1974; Klassen et al. 2000; Khan & Aurass 2002; Warmuth et al. 2004b), indicating the common nature of the underlying disturbance. The physical background of the relationship was explained by Uchida (1974): the coronal fast-mode MHD shock that propagates along “valleys of low Alfvén velocity” excites type II bursts in the corona, whereas the Moreton wave is a “surface track” of the shock front propagation (cf., Uchida 1974, and references therein).

Generally, the coronal large-amplitude MHD disturbance could be generated by flares as well as by CMEs, and quite likely, both types of processes happen (Vršnak et al. 2001). The excellent timing association of Moreton waves and type II bursts with the impulsive phase of associated flares (e.g., Harvey 1965; Švestka & Fritzoza-Švestkova 1974; Vršnak et al. 1995; Vršnak 2001; Klassen et al. 1999, 2003; Warmuth et al. 2005) strongly suggests that the waves are ignited by flares. This is also supported by a number of relatively well-defined correlations between various wave characteristics and the flare energy release characteristics (e.g.,

Cane & Reames 1988; Pearson et al. 1989; Magdalenic & Vršnak 2000; Vršnak 2001; Vršnak et al. 2001, and references therein), consistent with theoretical considerations (Vršnak & Lulić 2000a,b; Vršnak 2001).

Attempts to find analogous correlations between CME parameters and the characteristics of metric type II bursts have turned out to be much less successful, because the correlations are either absent or have a very low statistical significance (Reiner et al. 2001; Shanmugaraju et al. 2005). On the other hand, the significance of correlations increases if long-wavelength (dekameter-hektometer range, hereafter DH-range) type II bursts are compared with CMEs (Reiner et al. 2001), consistent with the generally accepted view that interplanetary (IP) shocks are driven by CMEs. At first glance, therefore, one might conclude that coronal shocks are generated by flares, whereas the IP ones are driven by CMEs. However, there is a certain fraction of coronal type II bursts that extend from the meter-dekameter wavelength range to the hektometer and kilometer range (e.g., Gopalswamy 2005), tracing the shock propagation from the corona out to the IP space. Since IP shocks are driven by CMEs, one has to conclude that a certain number of coronal disturbances are caused by CMEs. Following this argument Cliver et al. (1999) put forward the hypothesis that all coronal and IP shocks are driven by CMEs. The hypothesis finds support in several related studies, such as that of Biesecker et al. (2002), who demonstrated a close link between EIT waves and CMEs, the papers by Zarro et al. (1999) and Thompson et al. (2000a), where EIT dimmings were identified as the source regions of CMEs, and the study by Thompson et al. (2000a), where a close relationship between EIT dimmings and waves was demonstrated.

Unfortunately, even detailed case studies have not provided a clear answer to the question of whether a given coronal wave is driven by a CME or if it is ignited by a flare. Some aspects of the wave-flare/CME relationship (timing, spatial relationship, wavefront shape, etc.; for details see, e.g., Hudson et al. 2003; Warmuth et al. 2004a,b) in some well studied events strongly favor the flare-ignited scenario. However, the situation is complicated by the synchronization of the CME acceleration phase and the impulsive energy release in the associated flare (Zhang et al. 2001, 2004; Vršnak et al. 2004b, and references therein). That is the main reason why statistical (e.g., timing) analyses, as well as most case studies, cannot lead to a straightforward and unambiguous conclusion about the origin of coronal waves, as pointed out by Cliver et al. (2004). Obviously, a much more meticulous and systematic data analysis is required, including a more careful implementation of the theoretical constraints.

In this paper we utilize measurements of the large-scale coronal wave observed between 09:53 and 10:15 UT on 3 November 2003 to perform data analysis to be as detailed as possible and to confront the CME-driven and flare-ignited scenarios with the observations. This event offered a comprehensive multi-wavelength study, since it was observed by various techniques from the radio wavelength range to hard X-rays (Sects. 2 and 3). This allows an analysis of the launch and propagation of the wave (Sects. 4 and 5) in the context of the evolution of the associated flare and CME (Sect. 6). The goal

was to better understand the relationship between these three phenomena (Sect. 7). An extended discussion of some relevant aspects is given in the Appendix.

2. The data

The morphology and kinematics of the $H\alpha$ wave signature was analyzed using Kanzelhöhe Solar Observatory (KSO) $H\alpha$ filtergrams (Otruba 1999; Otruba & Pötzi 2003; <http://www.solobskh.ac.at/>). The KSO routinely takes full-disk $H\alpha$ images with a time cadence of ~ 5 s and a spatial resolution of $2.2''/\text{pixel}$. When the flare-mode is triggered, off-band filtergrams at $H\alpha - 0.3 \text{ \AA}$ and $H\alpha + 0.4 \text{ \AA}$ are also taken, generally with a cadence of about 1 image per minute.

The propagation of the soft X-ray (SXR) wave signature was traced with the data gained by the Soft X-ray Imager (SXI; Hill et al. 2005; Pizzo et al. 2005; <http://sxi.ngdc.noaa.gov/>) onboard GOES-12. The maximum sensitivity of SXI is primarily in the temperature range 1–10 MK. For the present analysis we used two different SXI filters: “open filter position” (SXI-o; 2.9–3.4 MK) and the thin polyimide filter (3.8 MK). The spatial resolution of SXI images is $5''/\text{pixel}$.

In the EUV range the wave was observed in two Fe XII 195 \AA images of the Extreme-ultraviolet Imaging Telescope (EIT; Delaboudiniere et al. 1995; <http://umbra.nascom.nasa.gov/eit/>) aboard the Solar and Heliospheric Observatory (SoHO). This channel shows coronal structures at temperatures around 1.5 MK. The images have a resolution of $2.6''/\text{pixel}$ and a field-of-view extending to 1.4 solar radii.

Positions of radio sources at 432, 411, 327, 237, 164, and 151 MHz were measured from the Nançay Multifrequency Radioheliograph (NRH; Kerdron & Delouis 1997) data. The NRH provides 8 images/second at each frequency with a beam size of a few arcmin at the lowest two frequencies and around 1 arcmin at 327 MHz (for details see <http://bass2000.obspm.fr>).

The evolution of dominant NRH sources was compared with the corresponding features in the dynamic spectrum of the Potsdam-Tremsdorf Radiospectrograph, covering the range 40–800 MHz with a time resolution of 0.1 s (Mann et al. 1992; <http://www.aip.de/groups/osra/>). The AIP spectrum was supplemented by the 20–650 MHz spectrum of the Solar radiospectrograph Artemis-IV of the University of Athens (Caroubalos et al. 2001; <http://www.cc.uoa.gr/artemis/>), and 25–270 MHz spectrum of the Solar Radio Laboratory of Izmiran (<http://helios.izmiran.troitsk.ru/lars/LARS.html>).

In the microwave (μw) range we used the 0.8–4.5 GHz spectra of the RT4/5 spectrograph of the Astronomical Institute Ondřejov (Jiřička et al. 1993; <http://sunkl.asu.cas.cz/radio/sol1.htm>), and the spectrum of the PHOENIX-spectrograph of ETH Zürich covering the range 100 MHz–4 GHz (<http://www.astro.phys.ethz.ch/rag/>). The radio emission spectrum in the dekameter/hektometer (DH) range was provided by the Radio Receiver RAD2 (1.075–13.825 MHz) of the Radio and Plasma Waves

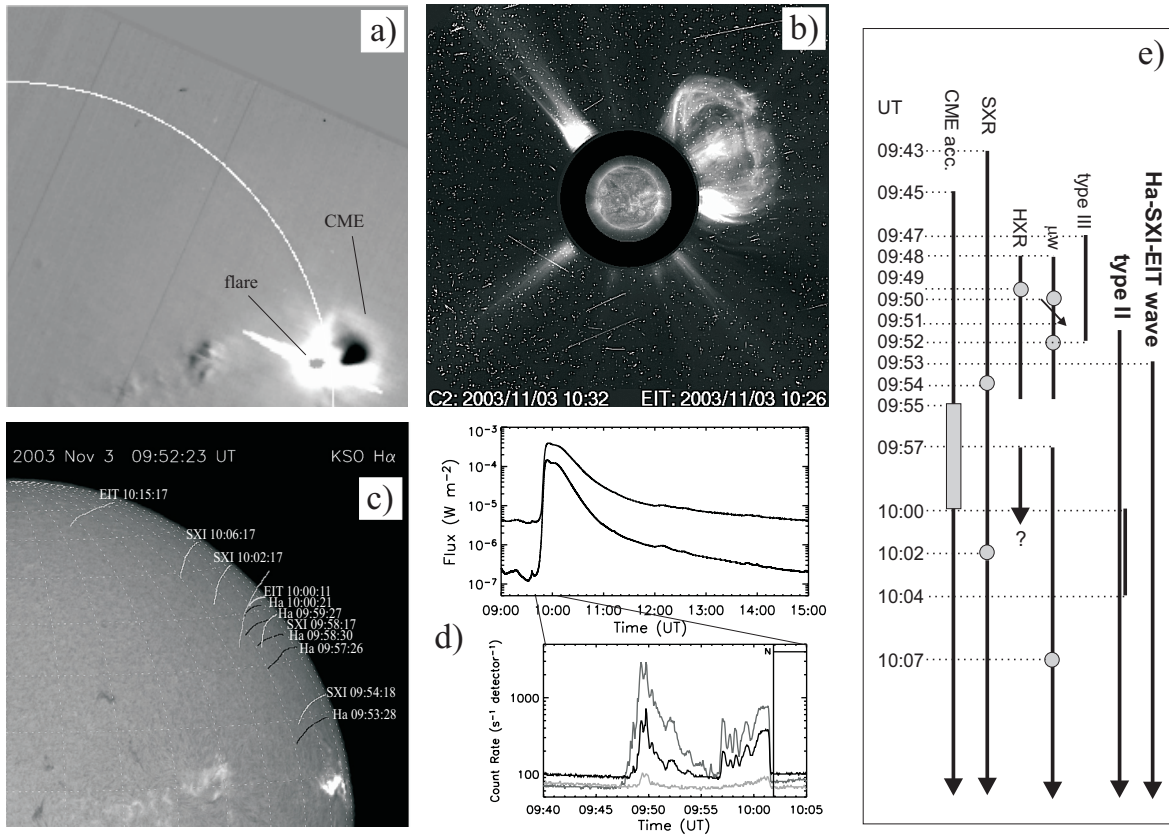


Fig. 1. The event of 3 November 2003: **a)** SXI-o difference image 09:54–09:50 UT, showing the flare and the CME take-off; **b)** LASCO-C2 image of the CME at 10:32 UT combined with EIT-Fe XII 195 Å image taken at 10:26 UT; **c)** KSO-H α , SXI, and EIT wavefronts (black, white, and gray lines, respectively) drawn on the H α filtergram taken at 09:52 UT; **d)** GOES 1–8 and 0.5–4 Å fluxes (upper panel) and the HXR burst recorded by RHESSI in the 50–100, 100–300, and 300–800 keV range. **e)** Schematic presentation of the event chronology; circles indicate maxima of bursts, the shaded rectangle at “CME acc.” indicates the CME maximum acceleration phase, the question mark denotes the end of the RHESSI measurements, the small arrow at “ μ w” indicates the drifting microwave feature, and the short line (10:00–10:04 UT) by the “type II” line indicates the “3rd” type II burst.

Instrument aboard the Wind spacecraft (Bougeret et al. 1995; <http://lep694.gsfc.nasa.gov/waves/waves.html>).

The development of the flare in SXR was followed by inspecting the SXR flux measurements in the 1–8 Å and 0.5–4 Å GOES channels and GOES-SXI images. The hard X-ray flare characteristics were inspected utilizing data from the Reuven Ramaty High Energy Solar Spectroscopic Imager (RHESSI; Lin et al. 2002; <http://hesperia.gsfc.nasa.gov/rhessidatacenter/>).

The characteristics and evolution of the underlying magnetic field structure were checked using the measurements performed by the Michelson Doppler Imager onboard SoHO (MDI; Scherer et al. 1995; http://soi.stanford.edu/science/obs_prog.html). Kinematics of the flare-associated white-light CME was measured from the LASCO-SoHO data (Large Angle Spectroscopic Coronagraph; Brueckner et al. 1995; http://cdaw.gsfc.nasa.gov/CME_list/).

3. General description of the event

The X3.9 two-ribbon flare of 3 November 2003 took place at N08W77 in the active region NOAA 10488 (Fig. 1). A detailed

description of the flare morphology and evolution is presented by Liu et al. (2004) and Veronig et al. (2005). The evolution of the flare-related radio type IV burst sources is described by Dauphin et al. (2005), whereas Vršnak et al. (2005) described the broad-band metric-wavelength radio signature of the coronal wave detected by NRH.

The SXR burst in the 0.5–4 and 1–8 Å GOES channels started by a SXR precursor lasting from 09:34 to 09:40 UT. The main SXR burst started around 09:43 UT and reached a double-peaked maximum at 09:54/10:02 UT (see the upper panel in Fig. 1d, and the schematic chronology in Fig. 1e). The decay of the SXR burst lasted more than 5 h.

The RHESSI measurements expose a complex HXR evolution (see the lower graph in Fig. 1d). The first impulsive HXR burst (>100 keV) began around 09:48 UT and showed a double-peaked maximum at 09:49:20/09:49:50 UT. The HXR flux decrease lasted until 09:57 UT when a new, extremely rapid rise occurred. The HXR activity stayed at a high level till 10:01:20 UT when the RHESSI spacecraft entered the Earth’s shadow. The RHESSI images reveal a rising loop-top source and two laterally expanding footpoint sources (Veronig et al. 2005), consistent with the standard dynamical-flare scenario. The two phases of the HXR burst and the double-peaked

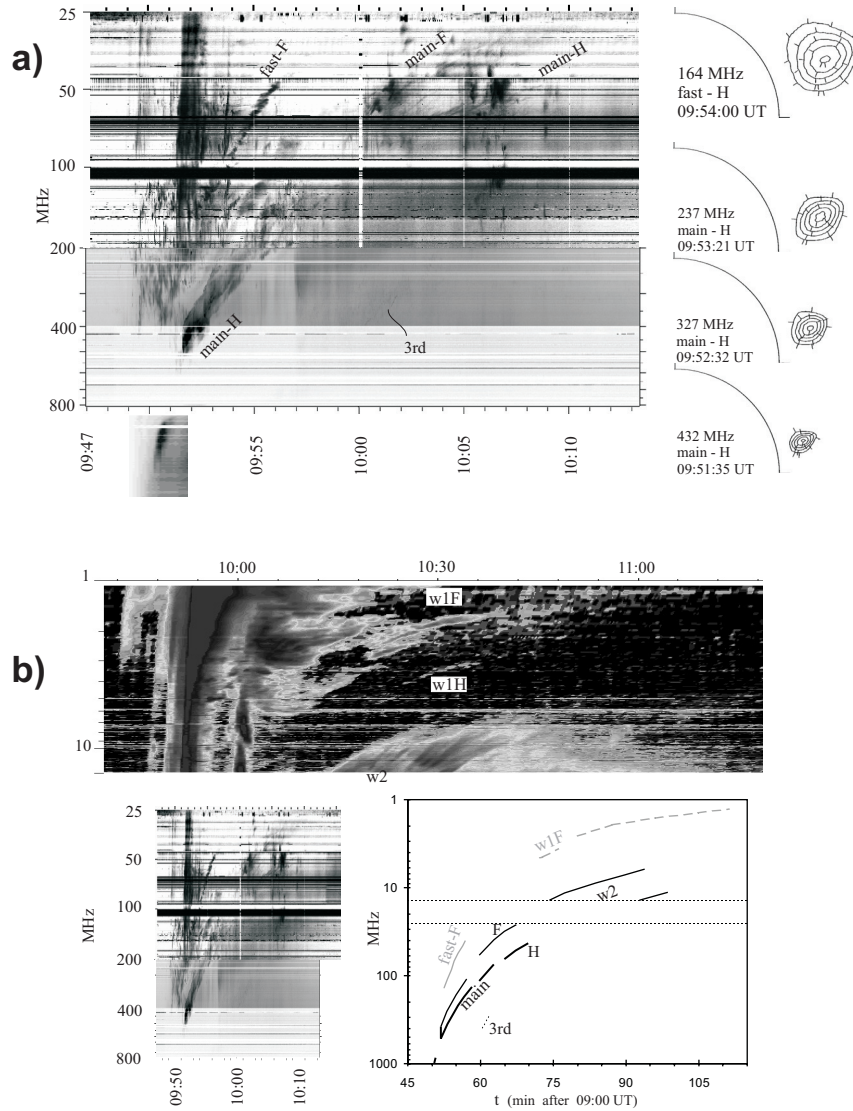


Fig. 2. **a)** The metric-range dynamic spectrum (AIP and Izmiran combined). The inset by the x -axis shows a part of the μw spectrum (1800–900 MHz, linear scale). On the right hand side, we show 432, 327, and 237 MHz main-lane harmonic-band NRH sources (lower three heliograms), and the 164 MHz fast-lane harmonic-band source (upper heliogram). Five contours from 20 to 95% of the maximum intensity are shown. **b)** Combination of the m-range and DH-range spectra. The dominant emission patterns measured from the μw to DH range are sketched in the inset. (For the used symbols see the main text).

maximum of the SXR burst show a Neupert-type relationship (Neupert 1968; see also, e.g., Veronig et al. 2002). The flare also produced γ -ray continuum emission.

The centimeter/decimeter range μw burst started around 09:48 UT and showed an even more complex evolution than the HXR burst. Still, two stages could be clearly identified, corresponding to the two HXR phases (see Dauphin et al. 2005). The main 3 GHz burst lasted until $\sim 10:15$ UT, with a prolonged decay lasting until ~ 11 UT.

Between 09:50 and 09:51 UT, the Ondřejov μw dynamic spectrum reveals a distinct feature, slowly drifting from 1.4 GHz towards lower frequencies (see the inset by the x -axis in Fig. 2a, and the small arrow at the “ μw line” in Fig. 1e). The drift rate amounts to $df/dt \equiv \dot{f} = 8\text{--}10 \text{ MHz s}^{-1}$, which gives the normalized drift rate $\dot{f}/f = 0.006\text{--}0.009 \text{ s}^{-1}$, as would be

expected if the $f(f)$ relationship for type II bursts were extrapolated to these frequencies (Vršnak et al. 2001, 2004a).

The dynamic radio spectrum in the decimeter/meter wavelength range (Fig. 2a) reveals numerous fast-drift bursts and a group of type III bursts that started around 09:47 UT and attained the highest intensity around 09:51–09:52 UT. The type III bursts extended from the meter wavelength range out to the dekameter/hectometer (DH) range, revealing the escape of electron beams into IP space (Fig. 2b).

As shown by Fig. 2a, a complex type II burst started at 09:51:30 UT around 600 MHz (harmonic band). The spectrum also shows the type IV burst whose continuum emission (according to the single frequency measurements) started around 09:47 UT. However, the spectrum reveals several groups of narrow-band bursts between 200 and 400 MHz already after 09:40 UT. At 09:57 UT the type IV emission showed

a sudden intensity enhancement (Fig. 2a), simultaneously with the impulsive revival of the HXR emission. The type II/IV burst complex continues out to the DH range (Fig. 2b) – it entered the Waves RAD2 frequency range (<14 MHz) at 10:12 UT and continued to drift down to ~ 5 MHz (Fig. 2b).

The flare appeared in conjunction with a bright, $\sim 100^\circ$ wide CME of a well-defined three-part structure (Fig. 1b). The take-off of the ejection could be traced only in the SXI running-difference images. We could not find any direct $H\alpha$ signature, implying that there was no “cold” material contained in the erupting structure at the lift-off. The SXI erupting feature showed a circular pattern similar to the one described by Vršnak et al. (2004b), where it is shown that such an SXR ejection represents the hot core of the erupting magnetic arcade (see, e.g., Lin et al. 2004). The effect of the eruption is seen in the EIT running-difference images in a form of coronal dimming above the limb and the disappearance of some of the pre-existing coronal loops in the northern part of the AR. The NRH type IV burst sources (before their emission was overwhelmed by the type II burst sources) traced the motion of the SXI ejection closely.

The CME kinematics could be followed in SXI images from 09:46 UT, when the summit of the SXI-CME was at $R = 1.13 \pm 0.01$ and had a velocity of about 100 km s^{-1} . Applying various polynomial fits and smoothing options to the height-time measurements of the SXI erupting feature (for details see, e.g., Maričić et al. 2004), we found that the acceleration maximum, $\sim 1000 \text{ m s}^{-2}$, was achieved between 09:55 and 10:00 UT (Fig. 1e at the “CME acc.” line).

The CME entered into the LASCO-C2 field-of-view at 10:06 UT with a velocity around 1100 km s^{-1} and was still accelerating ($a = 400 \pm 100 \text{ m s}^{-2}$). The CME moved through the C2/C3 field-of-view roughly along the position angle $PA \sim 300^\circ$, showing a certain northward offset from the corresponding radial direction. After attaining a velocity of 1400 km s^{-1} at $\sim 10:30$ – $10:40$ UT, the CME started to decelerate ($a = -20 \pm 10 \text{ m s}^{-2}$).

Besides the type II burst, the propagation of the coronal shock caused the wave signature in $H\alpha$, SXI, and EIT images (Figs. 1c and 3). Between 09:53 and 10:01 UT, the KSO $H\alpha$ -center, $H\alpha - 0.3 \text{ \AA}$, and $H\alpha + 0.4 \text{ \AA}$ movies reveal a relatively diffuse Moreton wave, propagating northwards from the flare site (Figs. 3a and 3b). In the SXI running-difference images (Figs. 3c and 3d) the wave could be traced from 09:54 to 10:06 UT. The EIT running-difference images show signatures of the associated EIT wave at 10:00 and 10:15 UT (Fig. 1f). The coronal wave also excited a broad-band (327–151 MHz) weak radio emission, whose northward propagation could be traced in the NRH heliograms between 09:54 and 10:15 UT at the height 0–200 Mm above the limb (Fig. 3e; for details see Vršnak et al. 2005). The “NRH-wave” signature was clearly distinguishable from the type II burst sources that were appearing at successively lower frequencies as transient narrow-band outbursts emitted from successively larger heights (Fig. 2a, right panels).

The LASCO running-difference images reveal one more global-scale signature associated with the coronal wave; the coronal streamers located at $PA = 310^\circ$ and 45° (NW and NE

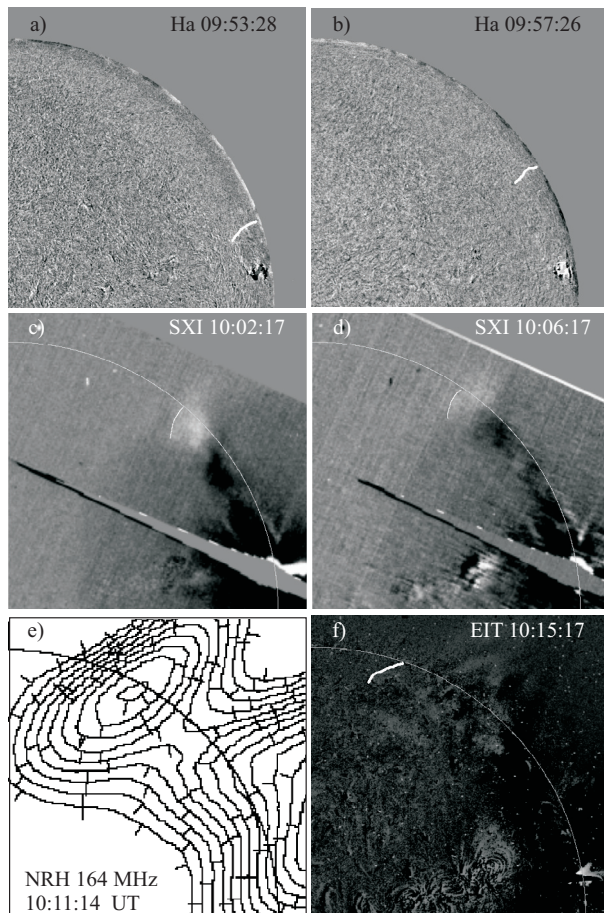


Fig. 3. Propagation of the coronal wave: **a)** and **b)** KSO- $H\alpha$; **c)** and **d)** SXI-o; **e)** NRH 164 MHz; **f)** EIT Fe XII 195 Å. Time is denoted in the images. In all panels except **e)**, running difference images are shown, and the wavefronts are indicated by white lines.

quadrants, respectively) were successively pushed in the clockwise direction, while the streamers at $PA = 255^\circ$ and 200° (SW quadrant) were displaced in the anti-clockwise direction. The displacement of the $PA = 310^\circ$ streamer occurred in conjunction with the $H\alpha$ /SXI/EIT signature, whereas the streamer at $PA = 45^\circ$ was on the other side of the north-pole coronal hole. The phenomenon can be interpreted by the refraction of the wave along the polar coronal hole boundary – the effect is sometimes directly observed in propagation of the SXI-waves (Warmuth et al. 2005). The displacement of the two southern streamers proves that at higher altitudes, the wave managed to propagate over or beside the high Alfvén velocity region in the southern part of active region NOAA 10488, as well as over or beside the high Alfvén velocity “dome” of NOAA 10486 located to the south of NOAA 10488.

4. The coronal wave signatures

4.1. Morphology

In Fig. 3 we illustrate the propagation of the coronal wave by showing several $H\alpha$, SXR, and EUV wavefronts (the superposition of wavefronts is shown in Fig. 1c) and the associated 164 MHz radio signature. The first wavefront position

was measured at the distance 125 Mm from the flare center in the $H\alpha$ filtergram taken at 09:53:28 UT. Before that, the wave contrast was not sharp enough to allow reliable identification of the wavefront. Between 09:55 and 09:57 UT, the contrast of the $H\alpha$ wave temporarily decreased again, so we could not measure the wavefront position in that interval.

After 09:57 UT, the contrast of the disturbance increased again, so we were able to measure the $H\alpha$ wavefront until 10:00:30 UT, when it was around 400 Mm from the flare. At this time the $H\alpha$ -wavefront position could be directly compared to the first EIT front (10:00:11 UT), and one finds that the two features were cospatial on the disc. The EIT feature was extended to above the limb, showing an inclination in the direction of motion (northwards). The plane-of-sky angle between the above-the-limb extension of the wavefront and the radial direction amounts to 20° – 30° . In the next EIT frame (10:15:17 UT) the wavefront reached the polar coronal hole boundary, located 780 Mm from the flare.

The first SXR wavefront could be identified in the SXI running-difference image 09:54:18–09:50:18 UT. Signatures of the wave were traced in the SXI images farther out than in the $H\alpha$ filtergrams, but not as far as in the EIT images (for similar examples see Warmuth et al. 2005). In this respect the SXI-wave range is similar to the range in which coronal waves are observed in He I 10 830 Å (Vršnak et al. 2002; Gilbert & Holzer 2004).

In the 151, 164, 237, and 327 MHz NRH-heliograms, the wave can be traced from 09:54 to 10:15 UT, covering practically the whole distance range from the first $H\alpha$ wavefront up to the last EIT signature at the border of the polar coronal hole. However, due to the low spatial resolution it is not possible to define the wavefront, so the NRH-wave kinematics will not be considered in the following analysis (for the measurements of the NRH-wave, see Vršnak et al. 2005). The NRH-wave was brightest when passing enhanced coronal structures at $PA \sim 285^\circ$ – 300° and 320° – 330° . At these locations, the radio-emission is prolonged, indicating that a local energy release was triggered by the disturbance.

4.2. Kinematics

The distance of the wavefront from the flare center, d , was measured along ten great circles on the solar surface, spanning an angle of 5° ; for details of the measurement procedure see Warmuth et al. (2001).

In Fig. 4a we present the $d(t)$ dependence of the wavefronts measured in the KSO- $H\alpha$, SXI, and EIT running-difference images. The mean velocity obtained from the linear least squares fit equals $\bar{v} = 490 \pm 10 \text{ km s}^{-1}$, and the back-extrapolation intersects the x -axis at 09:48 UT. Taking the $H\alpha$ measurements separately, we find that $\bar{v}_{H\alpha} = 642 \pm 3 \text{ km s}^{-1}$ and the x -axis intercept at 09:50 UT.

Figure 4a shows that the wavefront in fact decelerated: the quadratic least squares fit gives a mean deceleration of $\bar{a} = -340 \pm 15 \text{ m s}^{-2}$. The parabola intersects the x -axis at 09:50:30 UT, where the derivative adds up to $v_0 = 770 \text{ km s}^{-1}$. At the time of the first $H\alpha$ wavefront ($d = 125 \text{ Mm}$), the

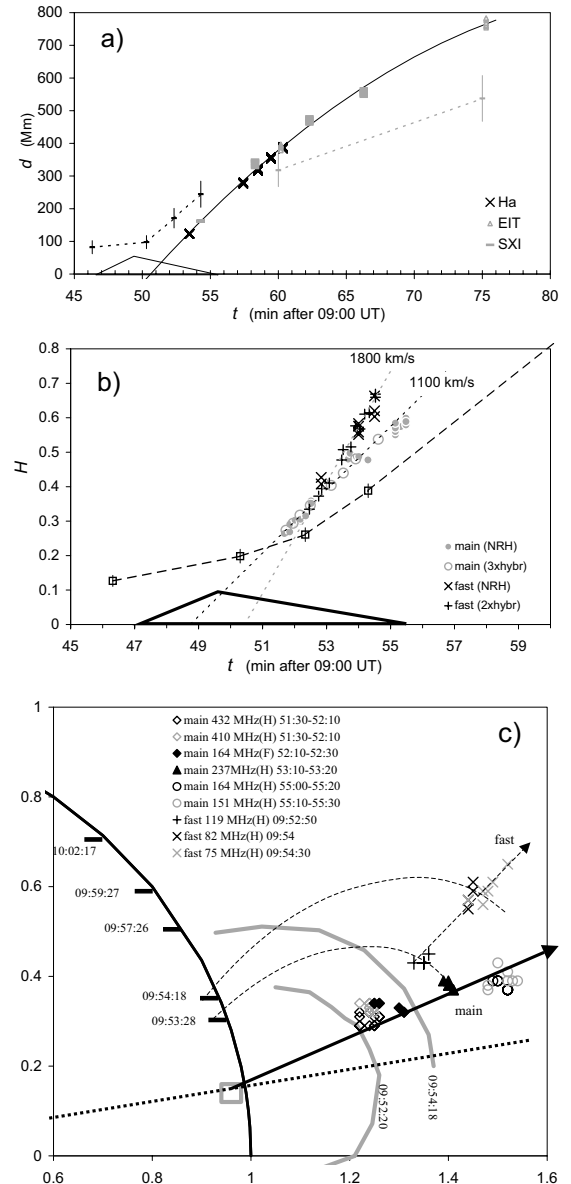


Fig. 4. a) Kinematics of the $H\alpha$, SXI, and EIT wavefronts. The first HXR burst is sketched by the large triangle at the x -axis. The propagation of the northern flank of the CME is shown by the dashed curve (black for SXI, gray for the EIT-dimming). b) Normalized heights, $H(t) = h/r_\odot$, of the main-lane and fast-lane NRH source (dots and crosses, respectively), together with the heights inferred from the radio spectrum (circles and pluses, respectively; for details see main text). The CME data are drawn by a thick-dashed line. c) Plane-of-sky positions of type II burst sources (see legend), $H\alpha$ /SXI-wave (dashes at the limb), and the leading edge of the SXI-CME (bold-gray lines). The x, y -coordinates are given in units of the solar radius. The bold-dotted line defines the position angle of the flare. The bold arrow depicts the direction of the CME propagation. Thin dashed lines connect (provisionally) the contemporaneous positions of the $H\alpha$ /SXI wave and the fast-lane source.

velocity decreases to 710 km s^{-1} , whereas at 10:15 UT, the velocity reads 270 km s^{-1} . The EIT wave velocity estimated directly from the two EIT wavefronts is 420 km s^{-1} .

The 2nd degree polynomial fit to the $H\alpha$ data gives $\bar{a}_{H\alpha} = -140 \pm 40 \text{ m s}^{-2}$. The fit intersects the x -axis at 09:50:30 UT,

when the fit-based velocity equals $v_0 = 695 \text{ km s}^{-1}$. At the time of the first $H\alpha$ wavefront, the velocity estimated from the fit decreases to 670 km s^{-1} , and at the time of the last measured $H\alpha$ wavefront (10:00:30 UT), the velocity is 610 km s^{-1} .

The power law fit of the form $d = \alpha(t - t_{0p})^\delta$, if applied to the combined $H\alpha$, SXI, and EIT data, gives $\delta = 0.66 \pm 0.01$ and the x -axis intercept 09:51:54 UT. Very similar values are obtained taking the $H\alpha$ data separately: $\delta = 0.68 \pm 0.01$ and the x -axis intercept 09:52:07 UT. Such values of δ are typical for coronal waves (Warmuth et al. 2004a). The velocity at 10:15 UT found from the fit through all data reads 370 km s^{-1} .

5. Type II burst

5.1. Spectral appearance

The type II burst started at 09:51:30 UT and showed a complex multi-lane spectrum (Fig. 2a). The most prominent emission lane, denoted as “main” in Fig. 2 (hereafter main-lane) started at 600 MHz (harmonic band). The lower frequency edge drifted from ~ 400 MHz down to ~ 30 MHz in about 20 min, giving an average drift rate of $\dot{f} = 0.3 \text{ MHz s}^{-1}$. In the range 100–50 MHz, the relative drift rate amounts to $\dot{f}/f \sim 0.0035 \text{ s}^{-1}$. The other distinct emission lane (denoted as “fast” in Fig. 2b, hereafter fast-lane) started around 09:52 UT at ~ 150 MHz (fundamental band), exposing a considerably larger frequency drift than the main lane ($\dot{f}/f \sim 0.0055 \text{ s}^{-1}$ in the 100–50 MHz range). The dynamic spectrum shows several more type II emission lanes and patches of weaker intensities, including the fundamental band of the main-lane and the harmonic band of the fast-lane.

The back-extrapolation of the type II emission pattern marks the drifting $\mu\nu$ emission recorded between 09:50 and 09:51 UT around 1 GHz, as shown in the inset below the x -axis in Fig. 2a and the dash on the x -axis of the $f(t)$ graph in Fig. 2b.

After the major type II burst, the AIP spectrum reveals an independent, weak type II burst pattern, drifting from 400 to 200 MHz between 10:00 and 10:04 UT (hereafter denoted as “3rd” type II burst).

5.2. Kinematics

The source of the main-lane emission was identified in all NRH frequencies, whereas in the case of the fast-lane we could identify only the source of the associated (weaker) harmonic-band emission, since the fundamental-band frequencies were lower than the lowest NRH-frequency (151 MHz). The measured plane-of-sky normalized heights ($H = h/r_\odot$) are shown in Fig. 4b, and the xy -plane positions are presented in Fig. 4c¹. Obviously, the main-lane and the fast-lane sources were located at different heights and moved in different directions. The fast-lane source was faster, consistent with the higher drift-rate in the dynamic spectrum.

¹ Figure 4c shows an interesting aspect of the relative position of the type II burst sources and the Moreton wave. If an observer were observing the AR on the solar disc close to the central meridian, he would see the type II burst source superposed on the Moreton wave, as happened in the case described by Khan & Aurass (2002).

The heights of NRH sources were compared with the source heights inferred from the dynamic spectra by applying different coronal density models: 1–10-fold model by Saito (1970), 1–3-fold model by Mann (1995), and 1–3-fold “hybrid-model” by Vršnak et al. (2004a). The best correspondence between the NRH data and the inferred values is found for the 2-fold hybrid model in the case of the fast-lane emission, and 3-fold hybrid model in the case of the main-lane (Fig. 4b)². Note, the hybrid-model is very convenient for the purposes of this study since it is defined by an explicit expression that smoothly joins the active region corona with the upper corona and IP space. Moreover, it is based on analysis of type II bursts (for details see Vršnak et al. 2004a), i.e., it characterizes coronal regions (whatever they may be) where type II bursts are excited (and not, e.g., the open-field corona from where type III bursts are emitted).

The linear least squares fit to the $h(t)$ data inferred from the dynamic spectrum of the main-lane emission in the period $<09:55$ UT gives a mean velocity of $\bar{v}_{\text{llm}} = 1100 \pm 10 \text{ km s}^{-1}$ and the x -axis intercept at 09:49 UT. Very similar values are obtained from the NRH data. The quadratic fit that includes all metric-range measurements (Fig. 5a) gives a mean deceleration of $\bar{a}_{\text{llm}} = -350 \pm 100 \text{ m s}^{-2}$, which is very close to the deceleration found for the $H\alpha$ /SXI/EIT wave signature (Sect. 4). The back-extrapolation to $h=0$ marks the “ignition time” at 09:50 UT when the “initial” velocity reads $v_{\text{llm}} \sim 1200 \text{ km s}^{-1}$. The power law fit of the form $d = \alpha(t - t_{0p})^\delta$ gives the exponent $\delta = 0.80 \pm 0.02$ and the x -axis intercept $t_{0p} = 09:50$ UT.

Using the two-fold hybrid model for the fast-lane emission, the inferred $h(t)$ dependence shows a constant propagation velocity. The linear least square fit in the interval $<09:55$ UT gives $\bar{v}_{\text{llf}} = 1800 \pm 100 \text{ km s}^{-1}$ and the x -axis intercept at 09:50:30 UT. The NRH data in the same period give the velocity 1500 km s^{-1} and the intercept at 09:49:30 UT.

The third distinct type II emission lane (denoted as “3rd” in Fig. 2b and drawn by pluses in Fig. 5a), obviously does not belong to the earlier type II burst complex. We could not identify the corresponding NRH sources due to the bright and very complex type IV burst emission pattern (Dauphin et al. 2005), which is further complicated by the NRH side-lobe images. The back-extrapolation of the emission to $h=0$ marks the abrupt onset of the second HXR burst at 09:57 UT.

At 10:12 UT a continuation of the metric main-lane type II burst and moving type IV burst entered into the frequency range of Waves-RAD1. It was a complex burst showing characteristics of a moving type IV continuum, superposed by several type II burst emission lanes (the emission complex denoted as w2 in Fig. 2b). The DH-range type II/IV emission lasted from 10:12 to 11:05 UT with the low-frequency edge drifting to lower frequencies and reaching the 5 MHz level at $\sim 10:50$ UT. In Fig. 5b we show (diamonds) the normalized radial distances $R = r/r_\odot$ of the radio source inferred from the spectrum by applying the 3-fold hybrid density model to the $f(t)$ measurements of the lower frequency edge of the type II/IV emission

² For evaluating the $R(t)$ dependence from spectral $f(t)$ data, we used the lower frequency edge of the type II burst emission (for details see Vršnak et al. 2001).

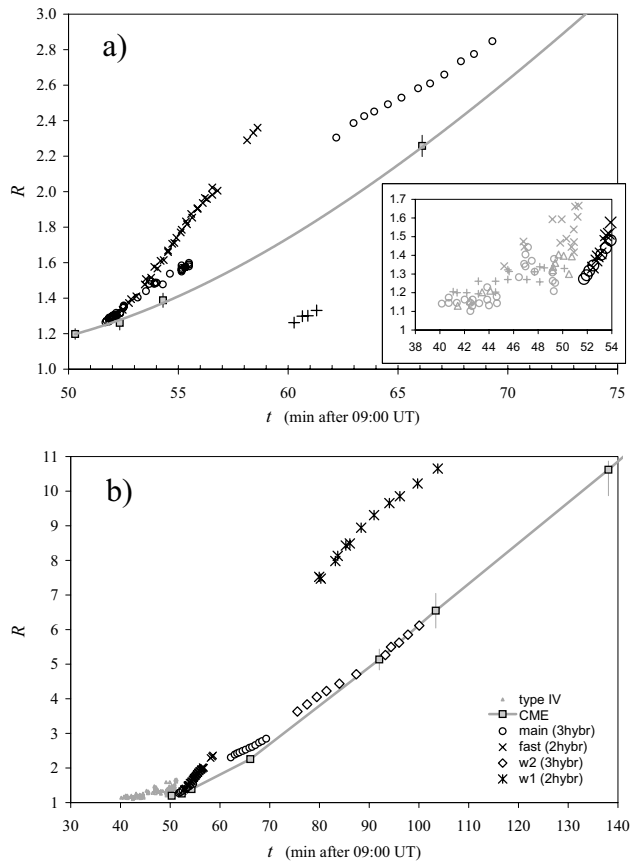


Fig. 5. The CME expansion (gray) compared with the propagation of the type II burst sources inferred by applying the three-fold and two-fold hybrid density model to the main-lane (circles) and fast-lane (crosses), respectively. **a)** Measurements in the metric wavelength range. In the inset we also present the NRH measurements of the moving type IV burst sources (gray: crosses – 164 MHz, pluses – 237 MHz, triangles – 411 MHz, circles – 432 MHz). **b)** Extension to the DH wavelength range (w1 – stars, w2 – diamonds). Positions of all NRH moving type IV sources in the interval 09:40–09:50 UT are shown by gray symbols.

complex (presumably the fundamental-band continuation of the metric main-lane emission; see Fig. 2b). The data are combined with the SXI and LASCO measurements of the CME and the metric-range radio measurements.

After $\sim 10:10$ UT, the Waves RAD-1 spectrum also shows a well defined band-split fundamental-band type II burst emission, drifting from $f \sim 6$ MHz down to $f \sim 1$ MHz at ~ 11 UT (denoted as w1F in Fig. 2b). The harmonic band can be also recognized (w1H in Fig. 2b), though is much weaker than w1F.

6. The wave–CME/flare relationship

All back-extrapolation options of the $H\alpha$ -SXI-EIT wave (see Sect. 4.2) mark the flare impulsive phase interval 09:48–09:52 UT, i.e., the first peak of the HXR and $\mu\nu$ burst and the highest activity of type III bursts. The same holds for the back-extrapolation of the main-lane and the fast-lane radio emission, as well as for all other associated weaker emission lanes. (Note that the back-extrapolated time practically does not depend on the choice of the density model – higher-density

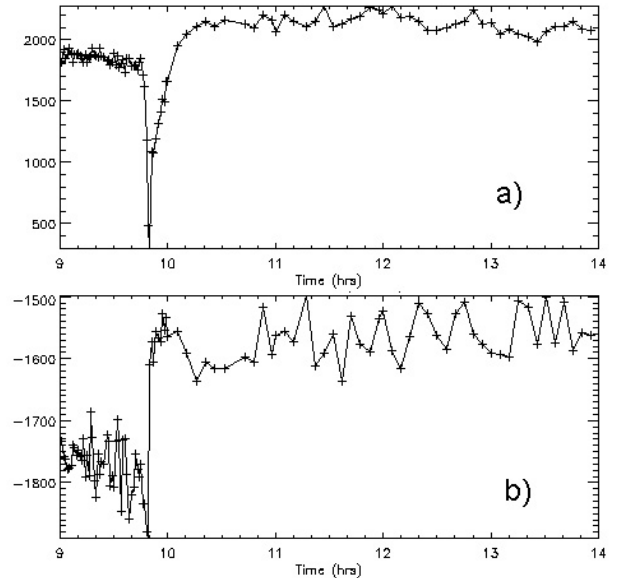


Fig. 6. Changes of the MDI signal in: **a)** north polarity HXR kernel and **b)** south polarity HXR kernel. The magnetic field (y -axis, in gauss) before and after the impulsive phase differs significantly. The sharp spike in a) is an artifact, probably caused by strong bombardment of energetic electrons beams. The sharp change happens during the HXR peak.

models result in larger source heights, which is compensated by the correspondingly larger velocities involved; for details see, e.g., Vršnak et al. 1995.) Hence, the wave–flare relationship is very distinctly defined.

On the other hand, the relationship between the wave and CME is much vaguer. In Fig. 4a the $H\alpha$ -SXI-EIT wave propagation is compared to the lateral expansion of the CME, which was measured in SXI difference images (black-dashed lines). The distances were determined by measuring the position angles of the intersection of the northern flank of the CME and the solar limb, which were then converted to the along-the-limb distances from the flare center. Consequently, the northward extension of the CME was underestimated, since it expanded more at larger heights. Moreover, the true extent of the CME might have been even larger, if the outer shells of the CME were out of the range of SXI temperatures (see, e.g., Fig. 6 of Vršnak et al. 2004b). In any case, in the period where the SXI measurements of the CME were possible, the wave was clearly behind the CME flank.

At the time of the type II burst onset (indicating the coronal shock formation) and the time of the first detected $H\alpha$ wavefront, the measured velocity of the lateral expansion of the CME amounts to about $600 \pm 100 \text{ km s}^{-1}$. The EIT/LASCO measurements show that the expansion slowed down later on (see the positions of the EIT dimming region in Fig. 4a), so that in the period 09:54–10:00 UT the velocity decreased to $\sim 250 \text{ km s}^{-1}$. Since the dimming is usually attributed to the interior of the CME structure, the dimming region probably lags behind the leading edge of the CME. Nevertheless, the overall trend indicates deceleration, which also continues in the LASCO-C2 field-of-view until $\sim 10:30$ UT, when the angular width of the CME stabilized at $\sim 100^\circ$. Figure 4a indicates

that the wave overtook the northern flank of the CME around 09:57 UT at the distance $d \sim 300$ Mm.

In Fig. 4b the heights of the type II burst sources are compared with the heights of the SXI-CME summit. Inspecting Fig. 4b, one finds that the main-lane, as well as the fast-lane, emission started very close to the tip of the SXI-CME. The offsets amount to 15 and 50 Mm. The plane-of-sky radial velocity of the SXI-CME summit at the time of the type II burst onset was 450 ± 50 km s⁻¹. At the same time, the inferred velocities of the fast-lane and main-lane sources were 1800 km s⁻¹ and 1100 km s⁻¹, respectively.

In the inset of Fig. 5a we compare the heights of type II burst sources with the heights of type IV burst sources; the latter could be reliably measured only until 09:51:30 UT, when they were overwhelmed by very bright type II emission. The inset shows that the type IV sources are found at distances up to $0.5 r_{\odot}$ ahead of the type II sources. Considering that the radio propagation effects (see Appendix A) should be the same at a given frequency, and comparing only the 411 and 432 MHz type IV burst sources with the initial type II burst heights measured at the same frequencies, one finds that the type IV sources reached the height of $R \sim 1.4$ already at 09:47 UT, whereas the main-lane burst started 4.5 min later at $R = 1.27$.

Finally, in Fig. 4c the overall situation is summarized by the xy -plane presentation of measurements. The figure outlines the most essential characteristic of the wave-CME relationship in the period before $\sim 09:55$ UT: the wavefront surface and the CME surface intersect each other. We depict this situation by provisionally drawing two dashed lines that connect the type II burst sources with roughly contemporaneous H α /SXI wavefronts. The lower one ($\sim 09:53$ UT) intersects a CME contour that should be interpolated between the CME contours measured at 09:52 and 09:54 UT, whereas the second one ($\sim 09:54$ UT) intersects the upper CME contour.

7. Discussion

7.1. Summary of observational results

Before interpreting the observations, we summarize the most relevant results:

- H α , SXI, and EIT signatures of the coronal wave follow the same (decelerated) kinematical curve;
- The CME motion can be traced in SXI images from 09:46 UT, when the summit of the SXI-CME was at $R = 1.13 \pm 0.01$ and had a velocity of about 100 km s⁻¹. The NRH data reveal a moving type IV burst ahead of the SXI-CME summit (the offset ΔR increased from $0.1 r_{\odot}$ at 09:42 UT to $0.5 r_{\odot}$ at 09:50 UT, corresponding to $v_{IV} \sim 600$ km s⁻¹).
- Back-extrapolations of the main-lane and fast-lane type II emission and the back-extrapolation of the H α -SXI-EIT wave converge into the interval 09:48–09:52 UT, which coincides with the strongest HXR peak and the strongest type III burst activity. Furthermore, the type II burst back-extrapolations match with the appearance of the drifting

$\mu\nu$ burst perfectly³. At the same time, the CME was at height $R \sim 1.2$, had velocity $v = 300$ – 400 km s⁻¹, and still did not attain the peak acceleration (~ 1000 m s⁻² at $\sim 09:55$ – $10:00$ UT);

- The appearance of two type II burst lanes reveals that one shock segment was formed in the corona at 09:51:30 UT at $R = 1.27$ (main-lane), and the second one at another place at 09:52:30 at $R = 1.33$ (fast-lane); the two sources were moving at a speed of 1100 and 1800 km s⁻¹, respectively. At that time the CME leading edge was at $R = 1.26$ – 1.30 and had velocity $v = 460$ – 510 km s⁻¹; i.e., it was only slightly behind the type II burst sources, and was considerably slower. The associated moving type IV burst sources are found up to $R \sim 1.7$, i.e., the CME-associated perturbation was ahead of the type II burst sources;
- The H α wavefront was first measured at 09:53:28 UT at a distance of $d = 125$ Mm from the flare center, with a speed of 670 km s⁻¹. At the same time, the northern flank of the CME was at $d \sim 200$ Mm, i.e., ahead of the H α wavefront. The lateral expansion speed of the CME was around 600 km s⁻¹, and was decelerating to become ~ 250 km s⁻¹ after $\sim 10:00$ UT.
- the inferred coronal shock surface was intersecting the leading edge surface of the SXI-CME
- The back-extrapolation of the “3rd” type II coincides with the onset of the second HXR burst at 09:57 UT. At this time the CME leading edge was already at $R > 1.5$.

7.2. General consideration

The formation of a coronal shock that excites a type II burst and occasionally a Moreton wave, generally requires some source motion that creates a large-amplitude wave whose leading edge would subsequently steepen into a shock due to a non-linear evolution of the disturbance (e.g., Landau & Lifshitz 1987; Mann 1995; Vršnak & Lulić 2000a). Such motion can be caused by the plasma-pressure or magnetic-pressure pulse created by the energy release in the flare (e.g., Parker 1961; Uchida 1974; Karlický & Odstrčil 1994; Vršnak & Lulić 2000b; Hudson et al. 2003), by small-scale fast ejecta from the flaring region (e.g., Giovanelli & Roberts 1958; Gopalswamy et al. 1997, 1999; Klein et al. 1999), or by the eruptive expansion of a CME (e.g., Gosling et al. 1976; Maxwell et al. 1985; Cliver et al. 1999, 2004, 2005; Mancuso & Raymond 2004). In any case, the time/distance needed for the shock formation is determined by the kinematics of the source region boundary, whereas the back-extrapolation of the shock motion marks the acceleration phase of the source region’s expansion (Vršnak & Lulić 2000a). Unfortunately, resolving the generating process is generally difficult, since the acceleration phase of a CME is often closely related to the impulsive phase of the associated flare (Zhang et al. 2004; Vršnak et al. 2004b, and references therein), whereas the small scale ejecta might be too dim to be observed (cf., Kim et al. 2005).

³ The set of impulsive features marked by the type II burst back-extrapolation are sometimes denoted as “type II burst precursor”; see Klassen et al. (1999).

7.3. The “3rd” type II burst

Bearing these problems in mind, the weak type II burst, which appeared closely associated with the second impulsive HXR enhancement (the feature denoted as “3rd” in Fig. 2b), deserves special attention. Although not really spectacular, this feature might be very important since it offers a unique possibility of identifying the ignition process with large confidence. At the time of the appearance of this late type II burst, the CME was already far out in the corona and was certainly not driving the related shock. Since there was no signature of another CME (and it is not likely that two impulsive CMEs are launched from the same region within a few minutes), the disturbance is to be attributed to the new impulsive energy release in the flare. Furthermore, we could not identify any signature for small-scale ejecta, which indicates that the coronal wave was ignited by the gas or magnetic pressure pulse (e.g., Karlický & Odstrčil 1994; Vršnak & Lulić 2000b) caused by the impulsive revival of the flare energy release.

7.4. The main event

7.4.1. One or two coronal shocks?

In the case of the major type II burst associated with the $H\alpha/SXI/EIT$ wave, the situation is not that simple. First of all, there were two distinct type II burst sources, moving at different speeds in different directions; for the statistical aspect of multi-lane type II bursts and historical overview see Shanmugaraju et al. (2005). Hence, first we have to resolve whether the two emissions were either due to two distinct shocks or due to a single shock with two emission-exciting segments. In the former case, we must look for two disturbance-generating events, whereas in the latter case we need only one.

Inspecting Fig. 4b, one finds that the main-lane back-extrapolation intersects the x -axis around 09:49 UT, whereas in the case of the fast-lane the x -axis intercept is at 09:50:30 UT. The time difference becomes even smaller if the quadratic fit is considered (Sect. 5.2) and/or if the source region of the disturbance is considered to be at some height above the solar surface. Figure 4a shows that the $H\alpha/SXI/EIT$ -wave associated disturbance was launched at about the same time. Bearing in mind all ambiguities in determining the radio-source heights (Sect. 6; see also Appendix A), as well as the accuracy of the $H\alpha/SXI/EIT$ -wave position measurements (Sect. 4), such a timing characteristic favors the one-wave scenario. This conclusion is also supported by the simple/single type-II-precursor drifting feature in the cm-wavelength range.

If we nevertheless consider the two-shock scenario, we have to take into account that the fast-lane shock was faster and was launched later than the main-lane shock. If the two shocks were propagating in similar directions, the fast-lane shock would catch up with the main-lane shock. The two shocks would merge, creating the discontinuity of a larger amplitude; i.e., the shock signature would show a sudden jump in the propagation speed. Since such an effect was not observed (in fact, the main-lane source was decelerating), the only possibility for the two-shock scenario is that the shocks

propagated along considerably different directions within strongly restricted solid angles, which prevented the interaction. Such propagation characteristics require additional constraints on the locations and dimensions of the source regions, as well as a very specific spatial pattern of the coronal Alfvén speed (hereafter, v_A). Since all of that is quite unlikely (though not impossible), we conclude that the observations are not supportive of the two-shock option (Occam’s razor).

In the following, therefore, we will concentrate on the scenario that includes only one metric-range coronal shock (i.e., we do not consider the DH-range upper corona here). Looking at Fig. 4c, it is not difficult to imagine a 3-dimensional shock surface that connects the $H\alpha/SXI/EIT$ -wave signature and the two type II burst sources. The observations imply that the propagation speed of the disturbance was not isotropic. It was higher in the direction of the shock segment, which excited the fast-lane emission, than in the direction of the main-lane source. The disturbance was still slower close to the solar surface. The difference can be interpreted straightforwardly by differences in the local Alfvén speed (e.g., Warmuth & Mann 2005). A higher Alfvén velocity associated with the fast-lane source is consistent with a somewhat delayed appearance of this emission⁴: the time/distance needed for the discontinuity formation is longer (whatever the source process is) if the wave propagates in a higher-Alfvén-speed environment (Vršnak & Lulić 2000a).

7.4.2. Flare or CME?

As is often the case, the type II burst and the $H\alpha/SXI/EIT$ -wave show a very well-defined timing correlation with the impulsive energy release in the flare. The back-extrapolation of the wave signatures coincides with the HXR peak to within one minute and fits very tightly to the μw drifting feature. Furthermore, the back-extrapolations of the propagation directions of the $H\alpha/SXI/EIT$ -wave and the type II burst sources intersect at the flare site. Thus, the measurements strongly support the flare-ignited scenario.

On the contrary, the CME-driven scenario does have a serious drawback, as the $H\alpha/SXI/EIT$ -wave was initially propagating behind the northern flank of the SXI-CME. Another observational discrepancy concerns the type II burst sources, which were initially located very close to the leading edge of the CME – the offset is much smaller than expected for either the piston-shock or bow-shock type of relationship (for the difference between piston-shock and bow-shock see, e.g., Vršnak & Lulić 2000c; Vršnak 2005; Warmuth 2005, and references therein). In addition, measurements of the sources of the moving type IV burst show that the CME-associated disturbance was already ahead of the type II burst sources by $\sim 0.5 r_\odot$ ⁵.

Hence, the observations do not favor the CME-driven scenario. In particular, the bow-shock option can be definitely

⁴ The delay after the main lane emission onset amounts to ~ 30 s. Note that the onset times of the type II burst emissions, i.e., the shock formation times, are the best-defined observational parameters.

⁵ The radio emission might have been tracing the true leading edge of the CME (e.g., Maia et al. 1999, 2000).

excluded, since it is not compatible with the low velocity of the CME at that time ($v < 400 \text{ km s}^{-1}$), since bow-shocks require “supersonic” drivers (Landau & Lifshitz 1987; Vršnak & Lulić 2000c). Moreover, the shock and the driver should move at comparable speeds (Vršnak & Lulić 2000c). The argument can be further strengthened by the fact that the $H\alpha$ /SXI/EIT disturbance and the type II burst shock were decelerating, while the CME was accelerating. We extend the discussion of the blast versus piston scenarios in Appendix B, where we confront the observations with further theoretical issues relevant for comprehension of the wave formation and propagation.

Finally, it is important to emphasize one more phenomenon observed during the impulsive phase of the flare, which could give a clue toward resolving the process of the wave ignition. The MDI measurements showed at 09:49 UT a strong transient perturbation of the Ni I 6767.8 Å spectral line at the site of the HXR flare kernels (Fig. 6). The perturbation resulted in an apparent, sharp drop of the longitudinal magnetic field strength at 09:49–09:50 UT. Some 30 min after that, the measured field strengths stabilized at values significantly different than before the pulse. The impulsive change of the MDI magnetic field signal at 09:49–09:50 UT is an artifact, probably caused by the variation of the Ni I 6767.8 Å line due to the bombardment of energetic electron beams (Ding et al. 2002; for similar events see Liu et al. 2005, and references therein). However, once the line profile stabilizes as the flare fades, the MDI measurements should be as good as they were before (Ph. Scherrer, private communication). Thus, the change in the MDI magnetic field data observed for hours after the flare, is indicative of a real effect related to the magnetic field. The associated change of the coronal field that occurred over the interval of a few minutes might be considered as a magnetic pressure pulse that could have ignited the large-amplitude MHD wave (Karlický & Odstrčil 1994).

8. Conclusion

The presented analysis shows that the physical relationship between the CME/flare and the coronal wave (shock) could be quite complex. In this particular event the comparison of measurements with the basic theoretical background (cf. Appendix B) provides strong evidence that the coronal shock that produced the Moreton wave and the associated type II burst emissions was generated by the energy release in the flare rather than by the CME expansion. Furthermore, the second energy release enhancement caused another shock that clearly could not have been driven by the CME.

Such an outcome contradicts the conclusion by Cliver et al. (2004) according to which *all* coronal shocks are (probably) driven by CMEs. Of course, our analysis does not imply that all coronal shocks are ignited by flares; it is quite likely that a significant fraction of the low-frequency metric type II burst (starting frequency below or around 100 MHz) are caused by CMEs, especially when the associated flare is weak (e.g., Thompson et al. 1998; Gopalswamy & Thompson 2000). Moreover, there is no *a priori* reason why exceptionally impulsive CMEs launched from very low heights (such as the CME of 6 November 1997, described by Zhang et al. 2001 and

Cliver et al. 2004) would not cause even high-frequency type II bursts, starting in the decimeter wavelength range.

Obviously, CMEs play an important role in the formation of coronal waves, as documented by, e.g., Biesecker et al. (2002), Thompson et al. (2000a), Cliver et al. (2004), etc. However, the presence of a CME does not necessarily imply the shock was launched and driven by the CME, as we have demonstrated in this paper. A similar conclusion was drawn also by Cane & Erickson (2005), who analyzed a number of events showing independent type II bursts in the metric and DH wavelength range, as well as by Shanmugaraju et al. (2005) who analyzed multiple type II bursts in the metric range. In this respect it should be noted that, even if a shock is ignited by a flare, the presence of a CME might still be a necessary condition (Cliver et al. 2004). That would imply that only two-ribbon flares are able to ignite shocks, most likely due to dynamic restructuring of the magnetic field and the abrupt formation of the reconnection outflow jets in the wake of CME at the onset of the fast reconnection.

Acknowledgements. We are grateful to the AIP, ETH-Zürich, GOES, Izmiran, NRH, RHESSI, SoHO, and Waves teams for operating the instruments and performing the basic data reduction, and especially, for the open data policy. The work of A.W. was supported by the DLR under grant No. 50 QL 0001. M.T. and A.V. acknowledge the support by the Austrian Science Fund (FWF grant P15344). MK acknowledge the support by Grant A3003202 of the Academy of Sciences of the Czech Republic. We are grateful to the referee, V. Pizzo, for constructive suggestions that led to significant improvement in the paper.

Appendix A: Coronal scattering and positions of radio sources

Coronal scattering, refraction, and/or ducting of the radio emission (e.g., Robinson 1983) could affect the observed position of radio sources and thus influence the measurements presented in Sects. 5.2 and 6. At 400 MHz the effect is expected to be small, but the apparent source positions at lower frequencies could be affected more significantly (the effect is systematically larger at lower frequencies). Bearing in mind that the comparison of the NRH and spectral data indicates rather high densities, we are inclined to believe that propagation effects might have caused an overestimation of the source-heights. That would imply that the decrease in the density is steeper than in the considered models, and consequently, that the heights and velocities are overestimated, whereas the deceleration is underestimated. Consequently, at low frequencies, the main-lane source would be placed behind the CME, while the offset between the fast-lane source and CME would become smaller.

On the other hand, if the radio-waves propagated through a homogeneous corona, the harmonic emission source would apparently be shifted to lower heights than the real ones. Since we have mainly measured the positions of the harmonic-band sources, this effect would increase the offset of the type II burst sources from the leading edge of the CME. However, such an effect would require a still higher-density model, which we believe is not realistic.

Since most of our NRH measurements were performed in the harmonic band, according to Robinson (1983) the

scattering on small-scale dense inhomogeneities (“fibers”) is the most important effect that could affect the propagation of the radio emission. However, since the 164 MHz harmonic-band source was located at a larger distance than the earlier fundamental-band 164 MHz source, one could also conclude that, in fact, the propagation effects were not really large (for details see, e.g., Duncan 1979), which is expected in the presence of streamer plasma and the absence of “fibers” (Robinson 1983).

Appendix B: An extended discussion of blast/piston scenarios

In Sect. 7.4.2 we briefly presented arguments in favor of the flare-ignited blast scenario, and showed that the interpretation in terms of the CME-driven bow shock is inappropriate. Yet, we may try to re-examine the observations to see if there is a way to somehow implement the scenario in which the CME acts as a spherical piston. If the $H\alpha$ /SXI/EIT-wavefront were really propagating within the CME body, that would definitely discard the option in which the wave was driven by the CME. However, positions of the northern flank of the CME were measured approximately at the limb, i.e., at a certain height above the solar surface (say, 15–20 Mm). Bearing in mind both that unfortunately we could not identify the CME footpoints and that in the lift-off stage CMEs show a “superexpansion” (Maia et al. 1999; Zhang et al. 2004), it is possible that the CME footpoints were rooted much more southwards than was the measured flank, e.g., in the AR itself. In this case the northern edge of the CME would have been strongly inclined to the solar surface. Consequently, the field lines in front of the northern edge of the CME would then be pushed northward/downwards (due to the photospheric line-tying). That could have caused the $H\alpha$ /SXI/EIT wave-like disturbance at the footpoints of the disturbed field lines (basically like in the model by Chen et al. 2005); i.e., the “wave” signature would be seen below the CME contour.

However, even such an explanation encounters serious problems. Firstly, the lower part of the northern CME flank at ~ 10 UT would have to be inclined for more than 80° – 85° from the normal to the solar surface, i.e., it would be almost lying on the solar surface. Secondly, a disturbance created in this way would not be related to the formation of the type II burst shock, since the disturbance on the coronal (free) part of the perturbed field lines would already have propagated far ahead of the CME. Both issues are not supported by observations, so we consider them as very unlikely.

The drawback regarding the location of the type II burst sources relative to the CME leading edge and the moving type IV burst sources could be removed ad hoc by claiming that the type II burst was emitted from the shock-surface flanks, which is an argument usually employed in similar situations (e.g., Cliver et al. 2004, and references therein). Although it is not difficult to imagine such a 3-D situation, let us note that such an ad hoc explanation is airy since there is no observational evidence to support it. Moreover, taking a reasonable shape of the shock front into account, along with the unavoidable offset between the shock front and the leading edge of the

CME⁶ (which is likely to be still ahead of the SXI-CME tip), it turns out that the emission site has to be located at a segment of the shock that is extremely far to the side of the CME.

Finally, there is an intrinsic physical discrepancy between the CME-driven scenario and the measurements (at least in this event) that is – although not so obvious – even more serious than the mentioned “first-glance drawbacks”. Namely, the CME acceleration phase was relatively long, lasting in total 40–60 min (Sect. 3). In such a situation, the shock should be formed at much larger distances and with much larger delay than observed (Vršnak & Lulić 2000a). For the starting frequency (fundamental band) of $f_F = 300$ MHz, the acceleration phase of the CME should be much more impulsive; e.g., the velocity of $1.2 v_A$ should be achieved in about 1 min (see Fig. 6f of Vršnak & Lulić 2000a). (Note that such a time scale was involved in the impulsive HXR burst, again favoring the flare-ignited scenario.)

Utilizing the measured CME kinematics, i.e., the acceleration time-profile and the maximum velocity achieved, the model by Vršnak & Lulić (2000a) provides an estimate of the time/distance needed for the shock formation. In particular, we can make use of Fig. 4b of Vršnak and Lulić (2000a), which simulates a piston moving at the velocity $v = 1.2 v_A$. Since the CME achieved a velocity of 1400 km s^{-1} , that value seems quite appropriate. From the graph, one reads that the shock should be formed close to the end of the acceleration stage, whereas the offset from the leading edge is comparable with the distance the piston has traversed in the meantime. Applying that to the observed situation, one finds that the shock should be formed around 10:10 UT at a height of 3–4 solar radii, i.e., at a radial distance $R \sim 4$ –5. Taking various coronal density models, one finds that such distances correspond to plasma frequencies 3–9 MHz. It is interesting to note that at 10:10 UT, the type II burst lane denoted as w1F appeared in the Waves-RAD1 spectrum at ~ 6 MHz (for similar spectral patterns of the metric and DH type II emission see Cane & Erickson 2005). Thus, it is quite possible that the w1F lane was excited by the CME-driven piston-shock that had just formed. Comparing in Fig. 5b the $R(t)$ curves of the CME and w1F, one finds a good correspondence with the pattern shown in Fig. 4b of Vršnak & Lulić (2000a).

On the other hand, there are also some aspects of the flare-ignited scenario that have to be resolved. The main problem concerns the fact that, according to this option, the disturbance was created after the eruption had already attained considerable velocity, so the wave evolution must have been strongly affected by the plasma flows associated with the CME expansion. In such an environment, it may happen that the wave profile never steepens into a shock.

The fastest flows associated with the eruption are associated with the leading edge of the CME. Ahead of the CME, the MHD wave-elements that carry information about the past kinematics of the CME have a velocity that is decreasing with the offset-distance from the leading edge of the CME; for the

⁶ Even in the case of the bow-shock, the offset should be quite large – most roughly, it should be comparable to the size of the CME (e.g., Russell & Mulligan 2002, and references therein).

evolution of the frontal-profile of the wave ahead of the piston and the associated plasma flow speeds see, e.g., Mann (1995), Vršnak & Lulić (2000a). In the wake of the CME, the flows are characterized by vortices (Cargill et al. 1996) that are formed to replenish the space behind the CME. Finally, at the flare site, the flows are presumably characterized by the reconnection flow-pattern consisting of converging horizontal inflows and the upward and downward outflow jets of hot plasma (e.g., Forbes & Malherbe 1991).

In this respect it is important to note that, at the flare onset, there has to be a period of time during which the reconnection system develops, i.e., a phase for formation of the reconnection jets (for characteristics of MHD waves propagating from the diffusion region and building the reconnection topology see, e.g., Biernat et al. 1998; Nitta et al. 2001). When the waves and jet “hit” into the low-lying magnetic structures they are abruptly deformed, which might launch the large-amplitude fast-mode MHD wave that subsequently develops into a shock. The outward propagating fast-mode shock can also be ignited directly at the current sheet in transition to the fast reconnection regime (Forbes 1988; Karlický 1988).

Bearing the lateral and radial expansion of the CME in mind, the presumed flare-ignited large-amplitude wave meets successively faster flows during its propagation, until reaching the leading edge of the CME where the flow-speed is highest. In such an environment the steepening of the wave profile is expected to be slower than in the stationary plasma, since the frontal profile-elements are faster than they should be in the stationary case. However, when the wave overtakes the leading edge of the CME, it comes to a situation where it meets successively slower plasma flows, so the relative speed between the farthest wave segments and those at the wave-amplitude maximum increases, i.e., the steepening of the profile becomes faster. Furthermore, it is very likely that, ahead of the CME body, the coronal Alfvén velocity is lower than within the CME⁷, and moreover, in the considered distance range it decreases with distance (Gopalswamy et al. 2001; Vršnak et al. 2004a; Warmuth & Mann 2005). Both characteristics of the background plasma are favorable for fast steepening of the wave into a shock.

The observed timing is consistent with such an interpretation. At the time of the flare’s impulsive phase ($\sim 09:49$ UT), the leading edge of the CME was at height $h \sim 100$ Mm and had a velocity of $v_{LE} \sim 300\text{--}400$ km s⁻¹. Taking $v_{II} = 1100$ km s⁻¹ for the velocity of the MHD disturbance (the velocity of the main-lane source), the time needed for overtaking the CME can be estimated roughly as $\Delta t = h/(v_{II} - v_{LE}) \sim 2\text{--}3$ min, consistent with the observed type II burst onset at 09:51:30 UT. Thus, the flare-ignited scenario provides a relatively simple explanation for the small offset between the type II burst’s onset-location and the leading edge of the CME (which on the other hand, turned out to be one of the major drawbacks of the CME-driven option).

As shown by Fig. 4 the wave propagation was faster in the radial than in the horizontal direction. Thus, the overtaking started at the CME summit, and soon the shock was formed ahead of the CME. At lower heights, the discontinuity probably had not developed yet. That might explain the low contrast of the Moreton wave, especially in the phase when the coronal wave was overtaking the low-lying flanks of the CME ($\sim 09:55\text{--}09:57$ UT, see Sect. 4.1).

References

- Biernat, H. K., Semenov, V. S., & Rijnbeek, R. P. 1998, *JGR*, 103, 4693
- Biesecker, D. A., Myers, D. C., Thompson, B. J., Hammer, D. M., & Vourlidas, A. 2002, *A&A*, 569, 1009
- Bougeret, J.-L., Kaiser, M. L., Kellogg, P. J., et al. 1995, *Space Sci. Rev.*, 71, 231
- Brueckner, G. E., Howard, R. A., Koomen, M. J., et al. 1995, *Sol. Phys.*, 162, 357
- Cane, H. V., & Erickson, W. C. 2005, *ApJ*, 623, 118
- Cane, H. V., & Reames, D. V. 1988, *ApJ*, 325, 895
- Cargill, P. J., Chen, J., Spicer, D. S., & Zalesak, S. T. 1996, *JGR*, 101, 4855
- Chen, P. F., Fang, C., & Shibata, K. 2004, *ApJ*, 622, 1202
- Cliver, E. W., Webb, D. F., & Howard, R. A. 1999, *Sol. Phys.*, 187, 89
- Cliver, E. W., Nitta, N. V., Thompson, B. J., & Zhang, J. 2004, *Sol. Phys.*, 225, 105
- Cliver, E. W., Laurenza, M., Storini, M., & Thompson, B. J. 2005, *ApJ*, 631, 604
- Caroubalos, D., Maroulis, N., Patavalis, et al. 2001, *Exper. Astron.*, 11, 23
- Dauphin, C., Vilmer, N., Lüthi, T., et al. 2005, *Adv. Space Res.*, submitted
- Delaboudiniere, J.-P., Artzner, G. E., Brunaud, J., et al. 1995, *Sol. Phys.*, 162, 291
- Ding, M. D., Qiu, J., & Wang, H. 2002, *ApJ*, 576, L83
- Duncan, R. A. 1979, *Sol. Phys.*, 63, 389
- Forbes, T. G. 1988, *Sol. Phys.*, 117, 97
- Forbes, T. G. 1991, *Sol. Phys.*, 135, 361
- Gilbert, H. R., Thompson, B. J., Holzer, T. E., & Burkepile, J. T. 2001, AGU Fall Meeting 2001, abstract SH12B-0746
- Gilbert, H. R., & Holzer, T. E. 2004, *ApJ*, 610, 572
- Giovanelli, R. G., & Roberts, J. A. 1958, *Australian J. Phys.*, 11, 353
- Gopalswamy, N. 2005, *Lect. Notes Phys.*, submitted
- Gopalswamy, N., & Thompson, B. J. 2000, *JASTP*, 62, 1457
- Gopalswamy, N., Kundu, M. R., Manoharan, P. K., et al. 1997, *ApJ*, 486, 1036
- Gopalswamy, N., Nitta, N., Manoharan, P. K., Raoult, A., & Pick, M. 1999, *A&A*, 347, 684
- Gopalswamy, N., Lara, A., Kaiser, M. L., & Bougeret, J.-L. 2001, *J. Geophys. Res.*, 106, 25261
- Gosling, J. T., Hildner, E., MacQueen, R. M., et al. 1976, *Sol. Phys.*, 48, 389
- Harvey, K. L. 1965, *JGR*, 70, 2961
- Harvey, K. L., Martin, S. F., & Riddle, A. C. 1974, *Sol. Phys.*, 36, 151
- Hill, S. M., Pizzo, V. J., Balch, C. C., et al. 2005, *Sol. Phys.*, 226, 255
- Hudson, H. S., Khan, J. I., Lemen, J. R., Nitta, N. V., & Uchida, Y. 2003, *Sol. Phys.*, 212, 121
- Jiříčka, K., Karlický, M., Kepka, O., & Tlamicha, A. 1993, *SPh*, 147, 203
- Khan, J. I., & Aurass, H. 2002, *A&A*, 383, 1018
- Klassen, A., Aurass, H., Klein, K.-L., Hofmann, A., & Mann, G. 1999, *A&A*, 343, 287

⁷ Presuming that the kinetic energy of CMEs is provided by the free-energy stored in the magnetic field one finds $\rho v^2/2 < B^2/2\mu$, i.e., the maximum CME speed v is lower than the Alfvén velocity in the CME body, v_A^* . In our case that gives $v_A^* > 1400$ km s⁻¹.

- Klassen, A., Aurass, H., Mann, G., & Thompson, B. J. 2000, *A&AS*, 141, 357
- Klassen, A., Pohjolainen, S., & Klein, K.-L. 2003, *Sol. Phys.*, 218, 197
- Karlický, M. 1988, *Bull. Astron. Inst. Czech.*, 39, 13
- Karlický, M., & Odstrčil, D. 1994, *Sol. Phys.*, 155, 171
- Kerdran, A., & Delouis, J. 1997, in *Coronal Physics from Radio and Space Observations*, ed. G. Trottet (Heidelberg: Springer-Verlag), 192
- Kim, Y.-H., Moon, Y.-J., Cho, K.-S., Kim, K.-S., & Park, Y. D. 2005, *ApJ*, 622, 1240
- Klein, K.-L., Khan, J. I., Vilmer, N., Delouis, J.-M., & Aurass, H. 1999, *A&A*, 346, L53
- Landau, L. D., & Lifshitz, E. M. 1987, *Fluid Mechanics*, 2d edn. (Oxford: Pergamon Press)
- Lin, J., Raymond, J. C., & van Ballegooijen, A. A. 2004, *ApJ*, 602, 422
- Lin, R. P., Dennis, B. R., Hurford, G. J., et al. 2002, *Sol. Phys.*, 210, 3
- Liu, C., Deng, N., Falconer, D., et al. 2005, *ApJ*, 622, 722
- Liu, W., Jiang, Y. W., Liu, S., & Petrosian, V. 2004, *ApJ*, 611, L53
- Maričić, D., Vršnak, B., Stanger, A. L., & Veronig, A. 2004, *Sol. Phys.*, 225, 337
- Magdalenic, & Vršnak, B. 2000, *Hvar Obs. Bull.*, 24, 1
- Maia, D., Vourlidas, A., Pick, M., et al. 1999, *JGR*, 104, 12507
- Maia, D., Pick, M., Vourlidas, A., & Howard, R. 2000, *ApJ*, 528, L49
- Mancuso, S., & Raymond, J. C. 2004, *A&A*, 413, 363
- Mann, G. 1995, *J. Plasma Phys.*, 53, 109
- Mann, A., Aurass, H., Voigt, W., & Paschke, J. 1992, *ESA SP-348*, 129
- Maxwell, A., Dryer, M., & McIntosh, P. 1985, *Sol. Phys.*, 97, 401
- Moreton, G. E., & Ramsey, H. E. 1960, *PASP*, 72, 357
- Narukage, N., Hudson, H. S., Morimoto, T., et al. 2002, *ApJ*, 572, L109
- Neupert, W. M. 1968, *ApJ*, 153, L59
- Neupert, W. M. 1989, *ApJ*, 344, 504
- Nitta, S., Tanuma, S., Shibata, K., & Maezawa, K. 2001, *ApJ*, 550, 1119
- Otruba, W. 1999, in *Third Advances in Solar Physics Euroconference: Magnetic Fields and Oscillations*, ed. B. Schmieder, A. Hofmann, & J. Staude. *ASP Conf. Ser.*, 184, 314
- Otruba, W., & Pötzi, W. 2003, *Hvar Obs. Bull.*, 27, 189
- Parker, E. N. 1961, *ApJ*, 133, 1014
- Pearson, D. H., Nelson, R., Kojoian, G., & Seal, J. 1989, *ApJ*, 336, 1050
- Pizzo, V. J., Hill, S. M., Balch, C. C., et al. 2005, *Sol. Phys.*, 226, 283
- Reiner, M. J., Kaiser, M. L., Gopalswamy, N., et al. 2001, *JGR*, 106, 25279
- Robinson, R. D. 1983, *Proc. ASA*, 5, 208
- Russell, C. T., & Mulligan, T. 2002, *Planetary and Space. Sci.*, 50, 527
- Saito, K. 1970, *Ann. Tokyo Astr. Obs.*, 12, 53
- Scherrer, P. H., Bogart, R. S., Bush, R. I., et al. 1995, *Sol. Phys.*, 162, 129
- Shanmugaraju, A., Moon, Y.-J., Cho, K.-S., et al. 2005, *Sol. Phys.*, accepted
- Švestka, Z., & Fritzo-Švestkova, L. 1974, *Sol. Phys.*, 36, 417
- Thompson, B. J., Plunkett, S. P., Gurman, J. B., et al. 1998, *GRL*, 25, 2465
- Thompson, B. J., Cliver, E. W., Nitta, N., Delannée, C., & Delaboudinière, J. P. 2000a, *GRL*, 27, 1431
- Thompson, B. J., Reynolds, B., Aurass, H., et al.: 2000b, *Sol. Phys.*, 193, 161
- Veronig, A., Vršnak, B., Dennis, B. R., et al. 2002, *A&A*, 392, 699
- Veronig, A., Karlický, M., Vršnak, B., et al. 2005, *A&A*, submitted
- Uchida, Y. 1974, *Sol. Phys.*, 39, 431
- Vršnak, B. 2001, *JGR*, 106, 25291
- Vršnak, B. 2005, *EOS*, 86, 112
- Vršnak, B., & Lulić, S. 2000a, *Sol. Phys.*, 196, 157
- Vršnak, B., & Lulić, S. 2000b, *Sol. Phys.*, 196, 181
- Vršnak, B., & Lulić, S. 2000c, *Hvar Obs. Bull.*, 24, 17
- Vršnak, B., Ruždjak, V., Zlobec, P., & Aurass, H. 1995, *Sol. Phys.*, 158, 331
- Vršnak, B., Aurass, H., Magdalenic, J., & Gopalswamy, N. 2001, *A&A*, 377, 321
- Vršnak, B., Warmuth, A., Brajša, R., & Hanslmeier, A. 2002, *A&A*, 394, 299
- Vršnak, B., Aurass, H., Magdalenic, J., & Gopalswamy, N. 2001, *A&A*, 377, 321
- Vršnak, B., Magdalenic, J., & Aurass, H. 2001, *Sol. Phys.*, 202, 319
- Vršnak, B., Magdalenic, J., & Zlobec, P. 2004a, *A&A*, 413, 753
- Vršnak, B., Maričić, D., Stanger, A. L., & Veronig, A. 2004b, *Sol. Phys.*, 225, 355
- Vršnak, B., Magdalenic, J., Temmer, M., et al. 2005, *ApJ*, 625, L67
- Warmuth, A., Vršnak, B., Aurass, H., & Hanslmeier, A. 2001, *ApJ*, 560, L105
- Warmuth, A., Vršnak, B., Magdalenic, J., Hanslmeier, A., & Otruba, W. 2004a, *A&A*, 418, 1101
- Warmuth, A., Vršnak, B., Magdalenic, J., Hanslmeier, A., & Otruba, W. 2004b, *A&A*, 418, 1117
- Warmuth, A. 2005, *Lect. Notes Phys.*, accepted
- Warmuth, A., & Mann, G. 2005, *A&A*, 435, 1123
- Warmuth, A., Mann, G., & Aurass, H. 2005, *ApJ*, 626, L121
- Wild, J. P., & McCready 1950, *Austral. J. Phys.*, 3, 387
- White, S. M., & Thompson, B. 2005, *ApJ*, 620, L63
- Zarro, D. M., Sterling, A. C., Thompson, B. J., Hudson, H. S., & Nitta, N. V. 1999, *ApJ*, 520, L139
- Zhang, J., Dere, K. P., Howard, R. A., Kundu, M. R., & White, S. M. 2001, *ApJ*, 559, 452
- Zhang, J., Dere, K. P., Howard, R. A., & Vourlidas, A. 2004, *ApJ*, 604, 420
- Zhukov, A. N., & Auchère, F. 2004, *A&A*, 427, 705